ORIGINAL ARTICLE

Decomposition of Displacement Field into the Irrotational and Solenoidal Component Using Fast Fourier Transform

Reza Bahrami Gorji [1], Mohammad Mohammadi [1], Bahador Makkiabadi [1,2*] (iD)

[1] Department of Medical Physics and Engineering, School of Medicine, Tehran University of Medical Sciences, Tehran, Iran

[2] Research Centre of Biomedical Technology and Robotics, Imam Khomeini Hospital Complex, Tehran University of Medical Sciences, Tehran, Iran

*Corresponding Author: Bahador Makkiabadi
  Email: B-makkiabadi@sina.tums.ac.ir

Abstract

Purpose: A new code based on Helmholtz decomposition is presented to separate longitudinal (pressure) and transverse (shear) components of a mixed wave field. This algorithm will help isolate shear or pressure components of an elastic wave to further concentrate on each specific wave and its physical characteristics, particularly in medical imaging instrument development and image processing techniques.

Materials and Methods: Using the combination of Fourier transform and Helmholtz decomposition, first, the mathematical basis of the work is prepared. After reaching a usable formula, this basis is embedded in the Code written in MATLAB program. Then, various test data containing shear and pressure waves were created and fed to the Code to evaluate its ability to decompose the displacements into the shear and pressure waves.

Results: This new algorithm successfully isolated the transverse and longitudinal wavefront of the mixed wavefield. The Code demonstrated 100% accuracy for separating the shear wave and more than 99% for the pressure wave. Moreover, the background noise was kept under 0.03% in every step.

Conclusion: The results show that using Helmholtz decomposition in Fourier space on 3D data can help decompose a displacement field into its irrotational and solenoidal components with high accuracy. A weak dependency on wave thickness and contrast was observed, but the algorithm's accuracy never fell below 99%.

Keywords: Helmholtz Decomposition; Fourier Transform; Vector Field; Longitudinal Waves; Transverse Waves.

1. Introduction

In biomedical imaging, image reconstruction is a critical part of the process. Especially in shear wave elastography, detecting shear waves passing through the tissue is a significant step. While shear waves do not have a predominant presence in biomedical imaging, in many research and development cases, it is essential to be able to focus on the physical characteristics of these waves. Therefore, wave decomposition can be essential in device development in shear wave-related medical imaging modalities.

To achieve this goal, it is possible to use Helmholtz decomposition [1] in Fourier space. A fair amount of knowledge can be borrowed from wave decomposition in geophysics and seismicity, where it is often used. In geophysics, producing images sometimes requires wave separation. Typically, the pressure and shear modes are separated and addressed separately. Otherwise, the two modes are blended on every component of the wave field, resulting in crosstalk and image artifacts [2].

A method of separation based on finite-difference extrapolation has been offered as a comparatively improved strategy [3]. This method was then further developed by rectifying the phase shift produced by the Helmholtz decomposition of the wavefield [4]. This method was extended from 2D to 3D, which splits the data into scalar pressure wave data and 3D vector shear wave data [5]. The 3-C (three Component) split shear wave data were then converted into scalar data for scalar migration [6].

Using the Helmholtz decomposition, Yan and Sava separated the waves in 2008 [2]. The divergence and curl processes alter the amplitude and phase of the split pressure and shear wave fields, resulting in incorrect amplitudes and phases in the migrated images.

Researchers are interested in vector wavefield separation methods to avoid the issues associated with wavefield separation techniques based on Helmholtz decomposition. They proposed one method to perform vector wavefield separation by solving an additional pressure or shear wave equation [7]. The introduction of the notion of vector wavefield separation in isotropic and anisotropic media occurred in the same year [8]. Since this method is done in the wavenumber domain, it is challenging to manage velocity models with significant variances. The wavefield separation operators were then

simplified by using the low-rank approximation and reducing the cost to a small number of FFT operations per time step. However, this approach is still time-consuming in heterogeneous media due to the substantial increase in the model size [9].

Researchers introduced a new algorithm based on vector Helmholtz decomposition in 2017 [10]. They perform vector wavefield separation in the space domain, which differs from the method developed earlier by Zhang and McMechan in 2010 [8]. This method begins with the solution of Poisson's equation before applying twice the spatial derivatives. Additionally, it generates pressure and shear wavefields with the same amplitude and phase as elastic wavefields. Later, an amplitude and phase correction technique was developed to avoid solving Poisson's equation, drastically reducing the computational cost of vector wavefield decomposition [11, 12].

Researchers theoretically analyzed the amplitude and phase distortion characteristics of wave fields in the decomposition of pressure and Shear waves based on Helmholtz decomposition in the time-space domain and formulated accurate wavefield decomposition and recomposition equations [13]. However, for some complicated structures, the proposed approach will be affected by energy leakage along the interface, reducing its precision.

Even though these studies provide considerable insights into wave-mode separation in anisotropic media, numerous obstacles remain, particularly in the computational implementation, if the proposed methods are implemented directly in practice. For instance, using nonstationary filtering to separate modes is computationally expensive, especially in three dimensions.

Based on the limits and expense of the current models and the limited data in biomedical research, it has been recommended to construct a MATLAB program capable of decomposing displacement fields in three dimensions.

This paper investigates the uses of Helmholtz decomposition in Fourier space and has specific needs and traits. Based on these conditions, it consists of an elastic wave emerging and propagating in a 2D axisymmetric environment, and the displacements in each direction were exported to be further analyzed. Since the simulation was done in a 2D axisymmetric environment, the exported data is a 2D cut in a cylindrical coordination system and must be taken back to its original form for analysis. Thus, the

objective was to create a code that could take the data, turn it back to its original form, perform the decomposition process based on the Helmholtz theorem in 3D, and assess the displacements made by each wave (pressure wave and shear wave).

2. Materials and Methods

2.1. Mathematical Basis

This work is based on Helmholtz's theorem, which states that any sufficiently smooth, rapidly decaying vector field in three dimensions can be resolved into the sum of an irrotational (curl-free) vector field and a solenoidal (divergence-free) vector field [14].

We can have a vector function F(r), of which we know the curl $\nabla \times F$ and the divergence $\nabla \cdot F$ in the domain and the fields on the boundary. Writing the function using the delta function in the form of (Equation 1)

$$\delta^3\left(r - r'\right) = -\frac{1}{4\pi}\nabla^2\frac{1}{|r - r'|} \tag{1}$$

Where $\nabla^2 := \nabla \cdot \nabla$ is the Laplacian operator, and with the identity $\nabla \times \nabla \times = \nabla\nabla \cdot -\nabla^2$, we have (Equation 2):

$$F(r) = \int_v F(r')\delta^3(r - r')dV'$$

$$= -\frac{1}{4\pi}\nabla^2\int_v\frac{F(r')}{|r - r'|}dV'$$

$$= -\frac{1}{4\pi}\left[\nabla\left(\nabla \cdot \int_v\frac{F(r')}{|r - r'|}dV'\right) - \nabla \times \left(\nabla \times \int_v\frac{F(r')}{|r - r'|}dV'\right)\right] \tag{2}$$

$$= -\frac{1}{4\pi}\left[\nabla\left(\int_v F(r') \cdot \nabla\frac{1}{|r - r'|}dV'\right) + \nabla \times \left(\int_v F(r') \times \nabla\frac{1}{|r - r'|}dV'\right)\right]$$

$$= -\frac{1}{4\pi}\left[-\nabla\left(\int_v F(r') \cdot \nabla'\frac{1}{|r - r'|}dV'\right) - \nabla \times \left(\int_v F(r') \times \nabla'\frac{1}{|r - r'|}dV'\right)\right]$$

In this project, instead of continuous functions, there are two 3D arrays containing displacements caused by an elastic wave (Figure 1), one of which contains displacements in the r-direction and the other in the z-direction. These arrays are treated as discrete functions.

Then, the conversion formulas can convert these displacements to cartesian (Figure 2). A vector P in cylindrical coordinates can be written by its unit vectors $P = P_\rho\hat{\rho} + P_\phi\hat{\phi} + P_z\hat{z}$. Cylindrical unit vectors can be converted to cartesian unit vectors using the following formula (Equation 3):

$$\hat{x} = cos\,\phi\,\hat{p} - sin\,\phi\,\hat{\phi}$$
$$\hat{y} = sin\,\phi\,\hat{p} + cos\,\phi\,\hat{\phi} \tag{3}$$
$$\hat{z} = \hat{z}$$

Thus, the displacement vectors in each pixel can be converted to their cartesian equivalent.

Note that since the simulation was done in a 2D axisymmetric environment (cylindrical coordinate system) and the exported data from COMSOL is a 2D cut by default, the data for the second dimension, the angle, is always zero.

For instance, for vector $P = P_\rho\hat{\rho} + P_\phi\hat{\phi} + P_z\hat{z}$, the conversion mentioned in Equation 3 gives Equation 4:

$$P_x = P_\rho\,cos\,\phi - P_\phi\,sin\,\phi$$
$$P_y = P_\rho\,sin\,\phi + P_\phi\,cos\,\phi \tag{4}$$
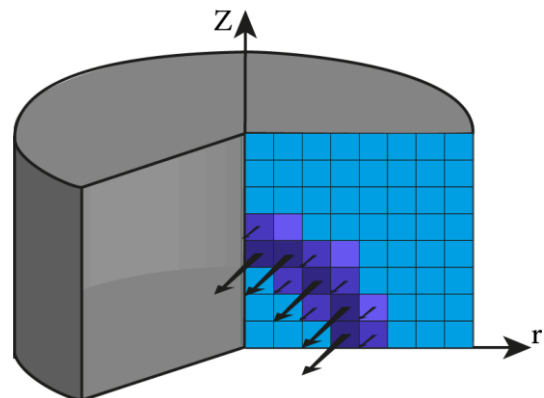$$P_z = P_z$$

Figure 1. Each pixel in the 2D cut contains the displacement of its center in a specific direction, r or z

In this project $\phi = 0 \rightarrow sin\,\phi = 0, cos\,\phi = 1$ and $P_z\hat{z}$ is the same in both coordinates; from 3 and 4 (Equation 5):

$$P = P_x\hat{x} + P_y\hat{y} + P_z\hat{z} = P_\rho\hat{\rho} + P_\phi\hat{\phi} + P_z\hat{z}$$

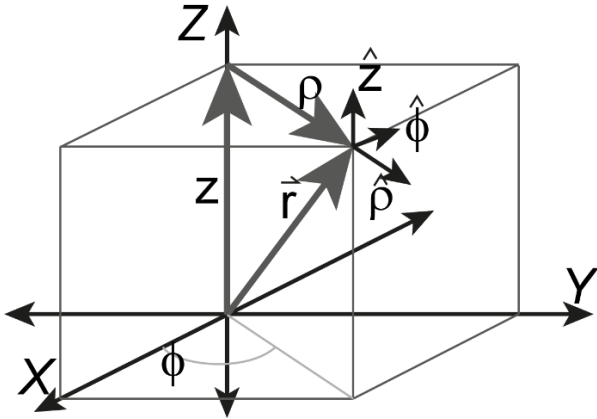$$P = P_x\hat{x} + P_z\hat{z} = P_\rho\hat{\rho} + P_z\hat{z}$$

(5)

Figure 2. Cylindrical unit vectors are given in the Cartesian coordinate system

The Fourier transformation will be used to estimate the differential and integral operators present in the Helmholtz theorem's mathematical basis. The rationale is to use the characteristics of the Fourier transform, which can solve a wide range of equations, from ordinary differential equations to complex curl or divergence equations.

In that sense, there is the following identity for the Fourier transform of a derivative (Equation 6):

$$FT[f^{(p)}(x)] = FT\left[\frac{d^p f}{dx^p}\right] = (ik)^p \hat{f}(k)$$

(6)

Thus, applying a Fourier transform to terms and equations involving derivatives replaces the differential components with a simple algebraic component f, which can be easier to solve.

If we write a function $f(x)$ as a Fourier integral, we have (Equation 7):

$$f(x) = \frac{1}{2\pi}\int \hat{f}(k)e^{(ikx)}dk$$

(7)

Differentiation with respect to x can be taken inside the integral, so (Equation 8);

$$\frac{df}{dx} = \frac{1}{2\pi}\int \hat{f}(k)ike^{(ikx)}dk$$

(8)

and we can recognize $ik\hat{f}(k)$ as the Fourier transform of the $\frac{df}{dx}$:

Also, the Fourier transform of the divergence of a vector field in three dimensions can be shown (Equation 9):

$$FT[\nabla \cdot v(x)] = ik_x \cdot \hat{f}(k_x)\vec{\imath} + ik_y \cdot \hat{f}(k_y)\vec{\jmath} + ik_z \cdot \hat{f}(k_z)\vec{k}$$

(9)

For the Fourier transform of the curl of a vector field, we have (Equation 10):

$$FT[\nabla \times v(x,y,z)] = ik_x \times \hat{f}(k_x)\vec{\imath} + ik_y \times \hat{f}(k_y)\vec{\jmath} + ik_z \times \hat{f}(k_z)\vec{k}.$$

(10)

Using this mathematical basis, the functions we need to calculate and perform the decomposition can be produced. If we have a vector field F, which is not bounded, F shall decay faster than 1/r; thus, the Fourier transform of F, denoted $\hat{f}$, is guaranteed to exist [15]. We apply the convention (Equation 11):

$$F(x,y,z) = \iiint \hat{f}(k_x)e^{ik_x x} + \hat{f}(k_y)e^{ik_y y} + \hat{f}(k_z)e^{ik_z z}dV_{k_{x,y,z}}$$

(11)

The Fourier transform of a scalar field is a scalar field, and the Fourier Transform of a vector field is a vector field of the same dimension. Consider the following scalar and vector fields (Equations 12-14):

$$\hat{f}_{\Phi_{x,y,z}}(k) = i\frac{k_x\hat{f}_x(k)}{\|k\|^2} + i\frac{k_y\hat{f}_y(k)}{\|k\|^2} + i\frac{k_z\hat{f}_z(k)}{\|k\|^2}$$

(12)

$$\hat{f}_{A_{x,y,z}}(k) = i\left(\frac{k_y\hat{f}_z(k)}{\|k\|^2} - \frac{k_z\hat{f}_y(k)}{\|k\|^2}\right)\hat{x} + i\left(\frac{k_z\hat{f}_x(k)}{\|k\|^2} - \frac{k_x\hat{f}_z(k)}{\|k\|^2}\right)\hat{y} + i\left(\frac{k_x\hat{f}_y(k)}{\|k\|^2} - \frac{k_y\hat{f}_x(k)}{\|k\|^2}\right)\hat{z}$$

(13)

$$\Phi(x,y,z) = \iiint \hat{f}_\Phi[(k_x)e^{ik_x \cdot x} + (k_y)e^{ik_y \cdot y} + (k_z)e^{ik_z \cdot z}]dV_{k_{x,y,z}}$$

$$A(x,y,z) = \iiint \hat{f}_A[(k_x)e^{ik_x \cdot x} + (k_y)e^{ik_y \cdot y} + (k_z)e^{ik_z \cdot z}]dV_{k_{x,y,z}}$$

(14)

Hence,

$$\hat{f}(k_{x,y,z}) = -[+ik_x\vec{\imath} + ik_y\vec{\jmath} \\ + ik_z\vec{k}].\hat{f}_\Phi(k_{x,y,z}) \\ + [ik_x\vec{\imath} + ik_y\vec{\jmath} + ik_z\vec{k}] \\ \times \hat{f}_A(k_{x,y,z}) \tag{15}$$

$$F(x,y,z) = \iiint [ik_x\vec{\imath} + ik_y\vec{\jmath} \\ + ik_z\vec{k}].\hat{f}_\Phi[(k_x)e^{ik_x.x} \\ + (k_y)e^{ik_y.y} \\ + (k_z)e^{ik_z.z}]dV_{k_{x,y,z}} \\ + \iiint [ik_x\vec{\imath} + ik_y\vec{\jmath} + ik_z\vec{k}] \\ \times \hat{f}_A[(k_x)e^{ik_x.x} \\ + (k_y)e^{ik_y.y} \\ + (k_z)e^{ik_z.z}]dV_{k_{x,y,z}} \tag{16}$$

Therefore, we conclude (Equation 17):

$$F(x,y,z) = -\nabla \cdot \Phi(x,y,z) + \nabla \times A(x,y,z) \tag{17}$$

It can be seen that the vector field is successfully written as a divergence-free and a curl-free component, as the Helmholtz theorem states.

Finally, in the Fourier space, one can have (Equation 18):

$$F(x)_{longitudinal} = k_x \cdot \frac{k_x \cdot \hat{f}(k_x)}{\|k_x\|^2} \tag{18}$$

and the same can be written for other directions, y and z. Also, it is correct to assume (Equation 19):

$$F_{Transverse} = F - k \cdot \frac{k \cdot \hat{f}(k)}{\|k\|^2} \tag{19}$$

since it is faster to compute the longitudinal component.

Now, to address the means of this approach, the Fast Fourier Transform can be used since its objective is to perform the Discrete Fourier Transform faster. It is known that executing DFT requires performing O(N2) complex operations for N data points, while the FFT reduces the number of computations for the same problem to O(NlogN) [10].

In MATLAB, the FFTN function is used since it computes the Discrete Fourier Transform (DFT) using a Fast Fourier transform algorithm in n dimensions.

2.2. Coding Procedure

The mathematical basics and necessary touches were implemented to successfully decompose an elastic wave to its transverse (shear wave) and longitudinal (pressure wave) components in 7 consecutive steps. These steps are: 1) creating the test data (or importing the data from COMSOL), 2) converting the 2D data to 3D, 3) changing the coordinate system, 4) performing Helmholtz decomposition, 5) Plotting the data, performing evaluations, 6) repeating the process with different input, and 7) Evaluation Using COMSOL input.

In order to have a specific set of data that can be checked quickly and precisely and remove any unwanted external interference, two simple 2D matrices were produced. Each of them contained displacements in a particular direction, r or z. These matrices are created as one side of a diameter cut from a cylindrical medium to replicate the exported data from a 2D axisymmetric simulation from COMSOL Multiphysics (Figure 3). Here are extra explanations to clarify the process further, with the help of the block diagram in Figure 8:

- The test data here is two matrices that we created and consist of displacements in perpendicular directions to model displacement fields with longitudinal (pressure waves) and transverse (shear wave) waves. On their own, the said matrices are just matrices with different values. However, it acts as a single displacement field with wavefronts of known size (displacement amplitude) and location when it goes through the procedure. Therefore, it is an ideal "test data" to test the performance of our algorithm.

- The synthesis of the test data is simple. We created two matrices with a specific value on specific arrays and zeroed
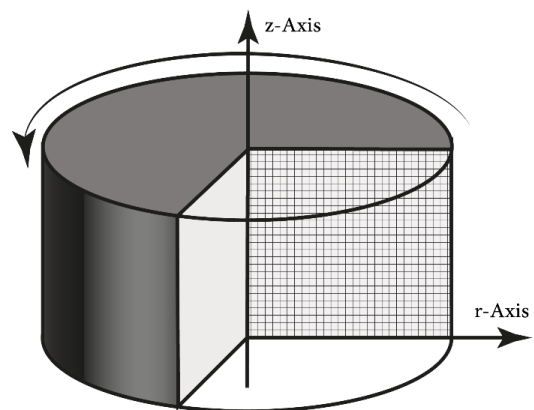

Figure 3. In a 2D axisymmetric model, our exported data is one side of a diameter cut from the cylindrical model

in on others. One of these matrices will be processed as a displacement map in the r-direction and the other as the displacement map in the z-direction. When, as part of the algorithm, they both revolve around the z-axis, one acts as a displacements field with a longitudinal wave in it (since the wave propagation is considered to be outward and the displacement is pointing outward or along the r-axis, as well) and the other acts as a displacement field with a transverse wave inside it (since the wave propagation is considered to be outward and the displacement is pointing upward, or along the z-axis, therefore perpendicular).

- The characteristics of the test data are discussed chiefly above. Plus, the nature of it, the size and direction of displacements, and their location are known. They also have known width (the number of pixels with displacement values).

- The reason for these characteristics consists of two parts: 1) to give them the properties of longitudinal or pressure waves, and 2) to keep all the essential data and remove any unwanted properties that are unnecessary to the algorithm and only complicate the results.

- Considering a wavefield is just a vector field, and a vector field is just a matrix with values and directions, the created test data should (in theory) cover every situation in the book. However, to make sure of the fact that practical properties (such as the width of the wave and the difference between the strength of the wave and background) do not affect the results too negatively, we tested the algorithm with test data with different properties in step 6 of the procedure.

Since our model and its interactions were done in a 2D axisymmetric environment, it contains crucial 3D information as well. Thus, the 2D data is converted into a 3D data set to maintain its integrity during decomposition. The primary tool here was the "revolve2D" function which is built in the k-wave toolbox for MATLAB. This function takes an m by n matrix, revolves it around the first dimension (the m dimension), and produces a 3D array. The new array has the same size in the first dimension, while the second and third dimensions have a 2n-1 size.

Note that if there is a wavefront with displacements in the z-direction, revolved around the z-axis, as there is in this project, it will end up with a wavefront resembling a transverse wave (Figure 4a) since the direction of displacement is perpendicular to the direction of propagation. Similarly, if a wave with displacements in the r-direction revolved around the z-axis, the final product will

resemble a longitudinal wave pattern since the propagation and displacements are in the same direction (Figure 4b). Thus, this test data will have two distinguished wavefronts, one longitudinal or pressure wave and one transverse or shear wave. In order to validate the final results, the longitudinal wave was purposefully designed with a smaller radius and less displacement, and the transverse wave with a larger radius and displacement.
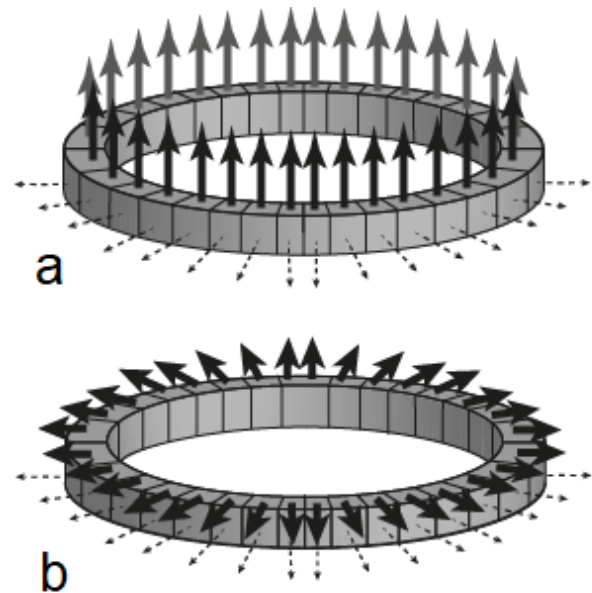

Figure 4. a) Displacements in the z-direction form a transverse wave after revolving. b) displacements in the r direction form a longitudinal wave

After running the first part of the program, two matrices are obtained, shown in Figures 5a and 5b below.
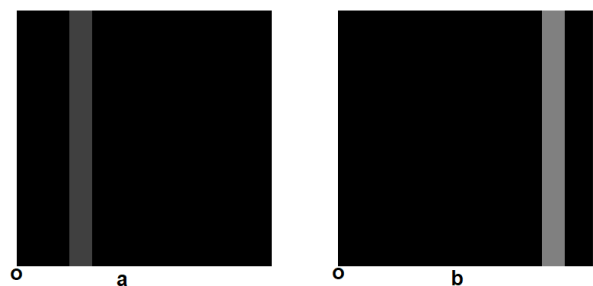

Figure 5. The 2D test data. a) The wavefront with the displacement in the r-direction represents the longitudinal waves (with a radius of 2 and smaller displacement). b) The wave with the displacement in the z-direction, representing the transverse wave (with a radius of 8 and larger displacement)

After revolving the matrices shown in Figure 5, we get a cube with a cylindrical wavefront inside it. Horizontally slicing this cube will result in 2D matrices with circular wavefronts, as shown in Figure 6. Furthermore, a plotted row from the middle of each slice (row 121) can be presented as a profile of the wavefronts, which can help to obtain the expected information (Figure 7).
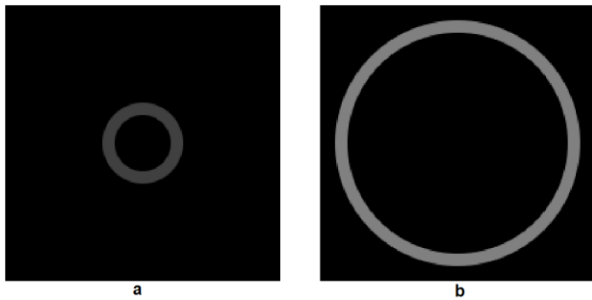

Figure 6. A horizontal cut in the z-axis of the test data, after being revolved, gives us a cylindrical (circle in 2D) wavefront. a) Wavefront with the displacement in the r-direction, which represents the longitudinal waves (with a radius of 2 and smaller displacement), b) Wave with the displacement in the z-direction, representing the transverse wave (with a radius of 8 and larger displacement)
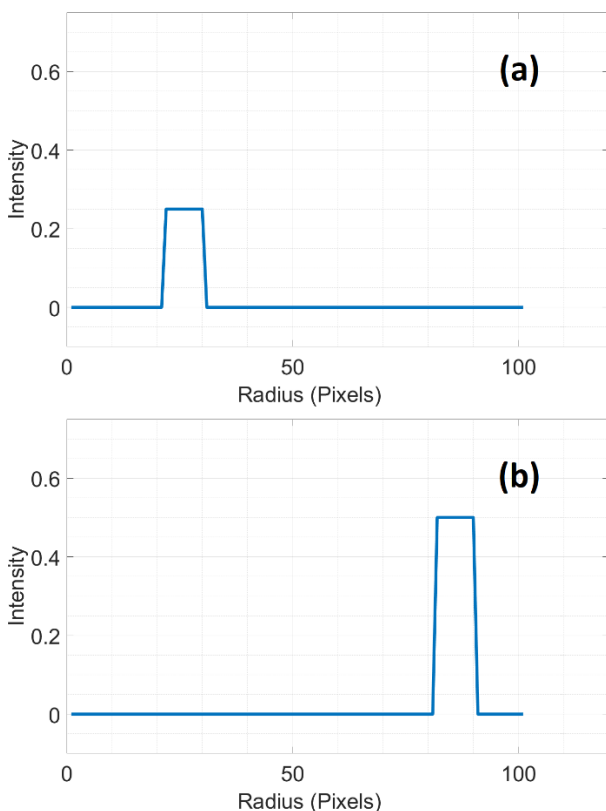

Figure 7. Profile of the wavefronts in the r (a) and z (b) directions

Since our simulation was done in a 2D axisymmetric environment, the data collected was in cylindrical coordinates. However, now it should be converted to cartesian coordinates to facilitate the rest of the process.

The displacements in the z-direction are the same in both coordinate systems, but the displacements in the r-direction will be decomposed into data in the x and y directions. Each displacement in the r direction can represent two separate displacements in the x and y directions using the sine and cosine operators based on each voxel's angle in reference to the original 2D cut. This step is the most complicated part of the program, where the decomposition of the test data is performed. The main reason for this complication is aligning the directions in the data set and the Helmholtz function.

Based on Equations 18 and 19, the decomposition process was performed on all three 3D arrays containing the displacement value in each cartesian direction, x, y, and z.

After obtaining two sets of three 3d arrays, one containing the displacements made by the longitudinal wave and the other containing the displacements from the transverse wave, each set of 3 arrays is combined to produce the displacements made by each wavefront in its entirety.

The last step is to extract one slice of each 3D array to present and do the necessary measurements. By creating a diameter cut and plotting the profile of each slice, the displacement made by each wavefront can be easily observed and measured.

With the evaluation cycle completed, new parameters were given to the data set to eliminate any link between parameters and results. Therefore, new data sets were created with I) reversing the position of transverse and longitudinal waves, II) higher contrast between the wavefronts (0.1 and 0.9 instead of 0.25 and 0.5), and III) thicker and thinner wavefronts.

Figure 8 is a block diagram showing the complete process with two entries. The algorithm was originally designed to take exported files from COMSOL (which needs different preparations, as seen in Figure 8) but now can create and examine a test wavefield as well. Finally, the Code is tested with a wavefield exported from COMSOL. This wavefield consists of two CVS files, one containing the displacements in the r-direction and the other containing the displacements in the z-direction. These CVS files are 2D matrices, and each column is a vector containing 14,641 pixels which are 121 squared. It also has 2703 columns, the number of time steps in COMSOL simulation. To

qualitatively evaluate the performance of the Code, a third CVS file is exported, which contains the total displacements of each voxel. By comparing the presence of each wavefront at a specific time during their propagation, the Code's ability to decompose and separately present the waves is evaluated.

3. Results

After running the program in its entirety, two subplots are obtained, one showing only the longitudinal wave and the other only the transverse or shear wave (Figure 9). Then, row 121 (the middle) is taken out and plotted as the profile for the wavefront and background. By plotting the profile of each

matrix, the displacement made by each wave was measured, as shown in Figure 10.

Here, we can use the data in matrices in Figure 9 and vectors plotted in Figure 10 to evaluate the accuracy of our algorithm. We can compare the obtained (decomposed) value for displacements with the input value, measure the noise in the background, and observe the waves visually.

The displacements of isolated shear and pressure waves were acquired to analyze the results quantitatively. Then, the mean values of the wavefronts were calculated, and for the shear wave, the mean displacement value was precisely 0.5, and for the longitudinal wave, it was 0.2490. Furthermore, three patches on the background were randomly
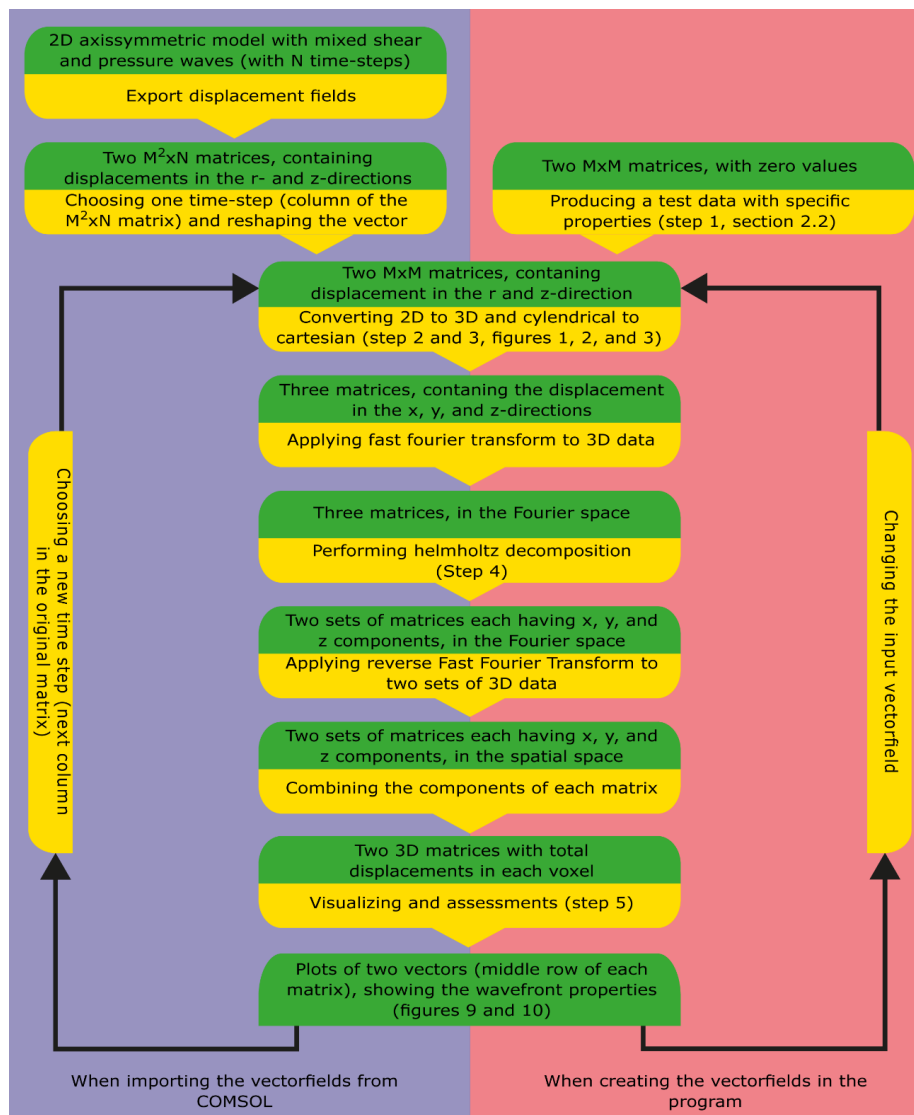

Figure 8. Block diagram of the entire process based on the origin of the test data, which can be COMSOL exported CVS files or two matrices of the wavefield created inside the algorithm
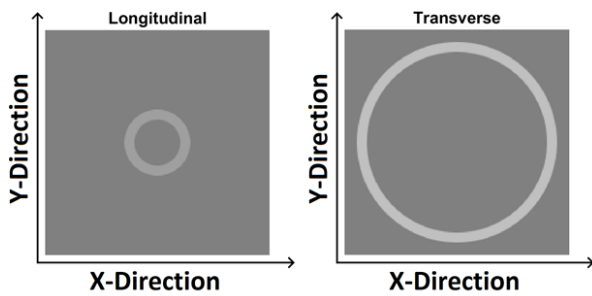
Figure 9. The final result of the Code gives us a completely separate transverse and longitudinal wave
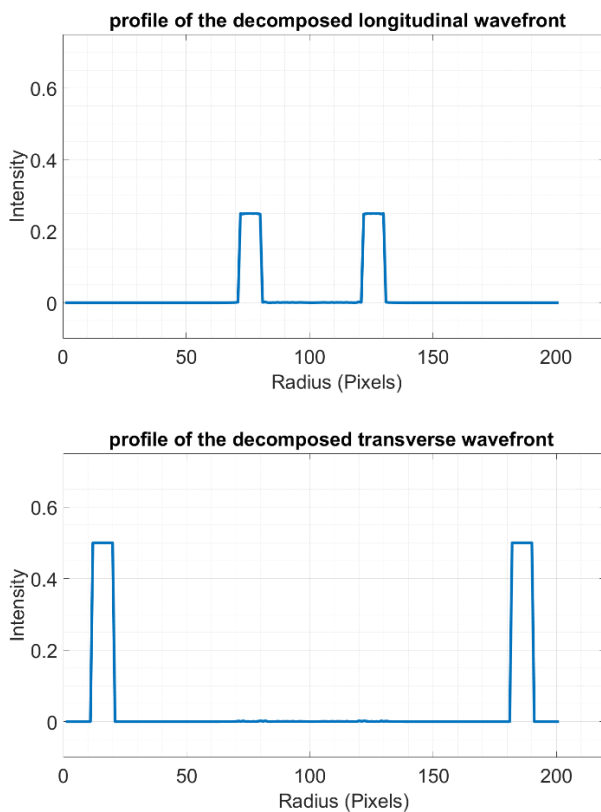

Figure 10. Displacement made by each wavefront after completing the decomposition

chosen, and the mean of the absolute values was calculated (using the mean function in MATLAB). For the shear wave, the average absolute value was calculated as 1.7427×10^{-4}; for the longitudinal wave, the background contained noises with an average absolute value of 1.7057×10^{-4}.

Next, to find any link between the location of the waves and the accuracy of our model, the locations were replaced, and the results showed the average shear wave and pressure wave displacements of 0.5 and 0.2495, respectively. Here, the average absolute

value of the background was slightly lower, calculated at 1.5081×10^{-4} and 1.5211×10^{-4}.

The next step was to evaluate any relationship between the wavefronts' contrast and the model's accuracy. The results of the decomposition code for different intensities of the waves are presented in Table 1.

Changing the thickness of the waves was the last step in evaluating the model and testing its accuracy against input wave parameters. Waves with relatively thinner and thicker wavefronts were created, and the responses are presented in Table 2.

A short description of each parameter in Table 1 is presented here:

- I) Average wave displacement for pressure wave: the average displacement of a point in space caused by the pressure wave passing through after decomposition. The set value in the primary model was 0.25 units, while after decomposition, it was slightly reduced to 0.249, which shows the model's accuracy.

- II) Average Absolute noise in pressure wave background: after the decomposition, we have two matrices. One contains the shear wavefront, and the other contains the pressure wavefront. Here we declare the average absolute value in the background (which is supposed to be zero, but after the decomposition, we expect to produce some noise) of the matrix that contains the pressure wave.

- III) Average wave displacement for shear wave: the same as (I), but for shear wave. The initial value for shear wave displacement was set to be 0.5 unit, and after the decomposition, it was precisely 0.5, which shows 100% accuracy for our algorithm.

- IV) Average Absolute noise in shear wave background: the same as (II) but for the matrix that contains the shear wave.

- V) Accuracy of the model for pressure waves: the ratio of the displacement of the decomposed pressure wave (I) to the set value for the same wave.

- VI) Accuracy of the model for shear waves: the ratio of the displacement of the decomposed shear wave (III) to the set value for the same wave.

- VII) Pressure wave Noise/Displacement: the ratio of the values in the background (II) to the

Table 1. Results were obtained from the model for various contrast intensities

Wavefront intensity	Average wave displacement for pressure wave	Average Absolute noise in pressure wave background	Average wave displacement for shear wave	Average Absolute noise in shear wave background	Accuracy of the model For pressure waves	Accuracy of the model For shear waves	Pressure wave Noise/Displacement	Shear wave Noise/Displacement
High-cont. 0.9 – 0.1	0.0996	6.8285×10^{-5}	0.9	6.9707×10^{-5}	99.6%	100%	6.86×10^{-4}	7.75×10^{-5}
High-cont. 0.8 – 0.2	0.1992	1.3657×10^{-4}	0.8	1.3941×10^{-4}	99.6%	100%	6.86×10^{-4}	1.74×10^{-5}
High-cont. 0.7 – 0.3	0.2989	2.0485×10^{-4}	0.7	2.0912×10^{-4}	99.6%	100%	6.85×10^{-4}	2.99×10^{-4}
Regular 0.5 - 0.25	0.2490	1.7057×10^{-4}	0.5	1.7427×10^{-4}	99.6%	100%	6.85×10^{-4}	3.49×10^{-4}
Low-Cont. 0.6 – 0.4	0.3985	2.7314×10^{-4}	0.6	2.7883×10^{-4}	99.6%	100%	6.85×10^{-4}	4.65×10^{-4}

Table 2. Results were obtained from the model for various thicknesses of the wavefronts

Wavefront Thickness	Average wave displacement for pressure wave	Average Absolute noise in pressure wave background	Average wave displacement for shear wave	Average Absolute noise in shear wave background	Accuracy of the model for pressure waves	Accuracy of the model for shear waves	Pressure wave Noise/Displacement	Shear wave Noise/Displacement
Thin (50%)	0.2479	6.2023×10^{-5}	0.5	5.7119×10^{-5}	99.16%	100%	2.50×10^{-4}	1.14×10^{-4}
Thin (75%)	0.2488	2.0524×10^{-4}	0.5	2.6245×10^{-4}	99.52%	100%	8.25×10^{-4}	5.25×10^{-4}
Regular (100%)	0.2490	1.7057×10^{-4}	0.5	1.7427×10^{-4}	99.6%	100%	6.85×10^{-4}	3.49×10^{-4}
Thick (125%)	0.2493	1.0039×10^{-4}	0.5	1.0573×10^{-4}	99.72%	100%	4.02×10^{-4}	2.21×10^{-4}
Thick (150%)	0.2495	7.2629×10^{-5}	0.5	7.5419×10^{-5}	99.8%	100%	2.91×10^{-4}	1.50×10^{-4}

displacement of the decomposed pressure wave (I). Theoretically, it should be zero (since the background of the test wave didn't have any noise). However, after the decomposition, it remains very close to zero, which shows the algorithm's accuracy.

- IX) Shear wave Noise/Displacement: the ratio of the values in the background (IV) to the displacement of the decomposed shear wave (III). Theoretically, it should be zero (since the background of the test wave didn't have any noise). However, after

the decomposition, it remains very close to zero, which shows the algorithm's accuracy.

The pictorial output of the Code for some of the variations is presented in Figures 11 to 14. They are the compressed versions of Figures 7, 9, and 10, with different inputs to eliminate any link between the properties of the input wave or created wave and the results and accuracy of the Code.
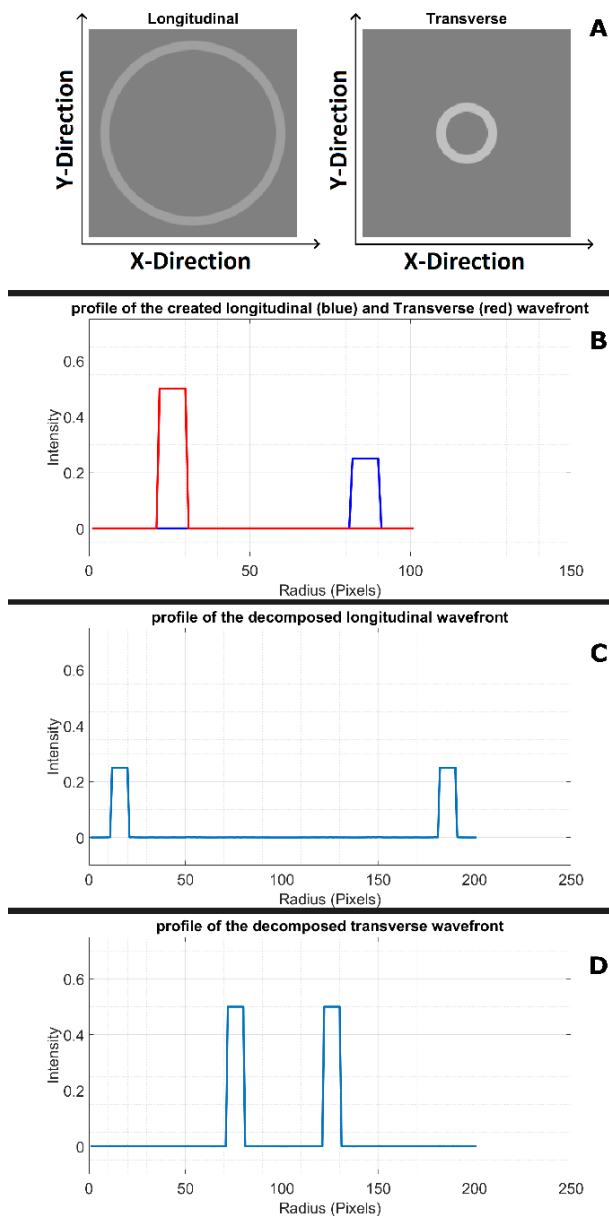
As the final step in evaluating the algorithm's performance, the input wavefield is changed to two CVS files exported from COMSOL, as discussed at the end of section 2. By observing the total displacement file, the pressure wave can be seen at the earlier stages of the simulation due to its faster propagation velocity (Figure 15). However, the shear wave can't be seen at the final time steps because the wavefield is full of echoes and residual waves.

The output of the algorithm can be seen in Figures 16 and 17.

Figure 11. The code output for the reversed location for the transverse and longitudinal waves. A) The image of the completely separated transverse and longitudinal waves. B) Profile of the created transverse and longitudinal waves. C) Profile of the decomposed longitudinal wavefront. D) Profile of the decomposed transverse wavefront
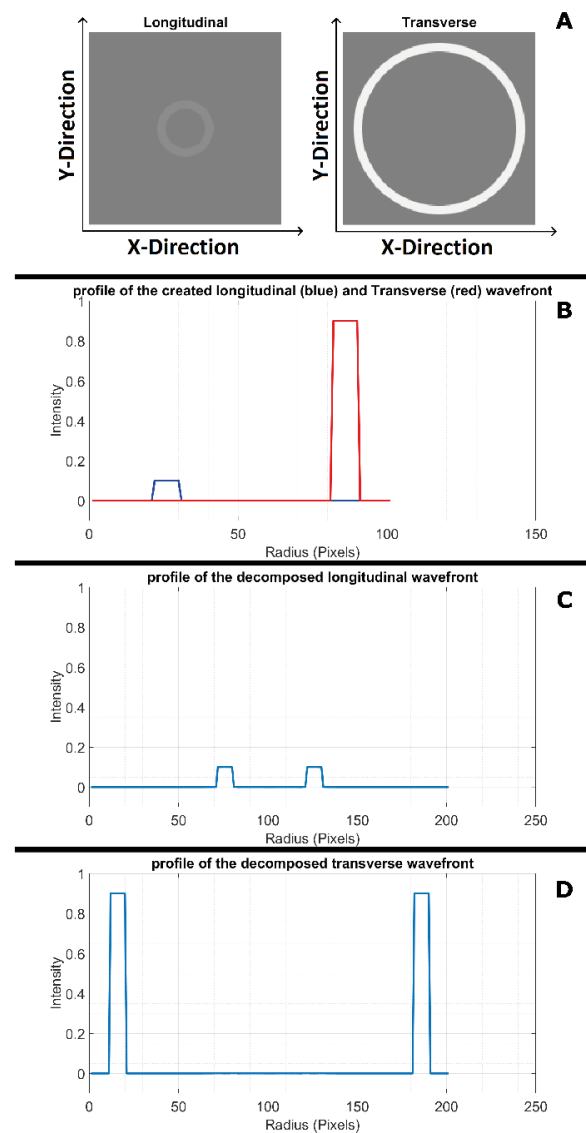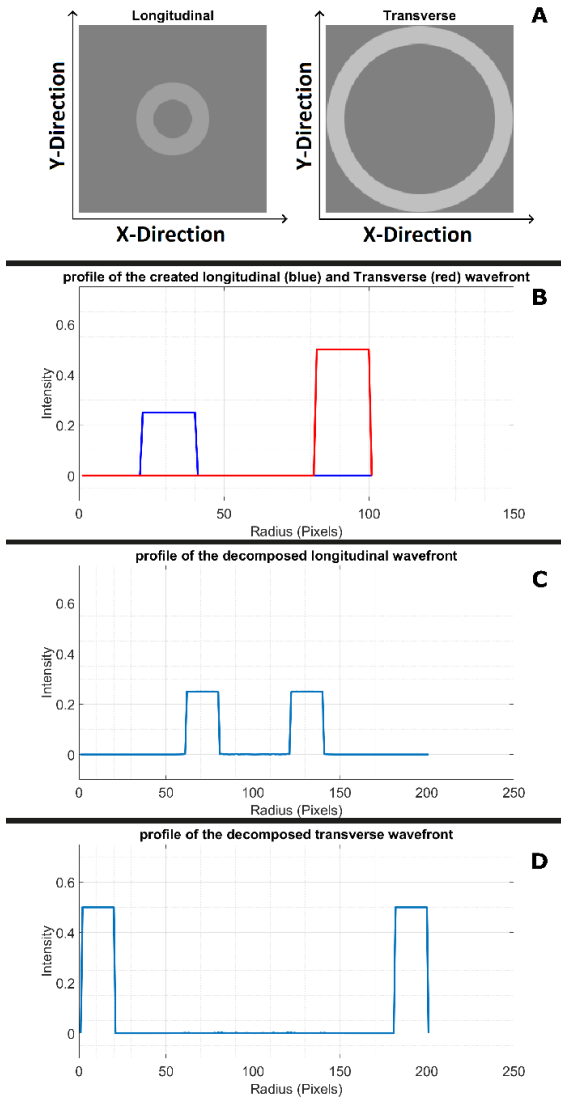

Figure 12. The code output for higher contrast (0.1 and 0.9) for the longitudinal and transverse waves, respectively. A) The image of the completely separated transverse and longitudinal waves. B) Profile of the created transverse and longitudinal waves. C) Profile of the decomposed longitudinal wavefront. D) Profile of the decomposed transverse wavefront
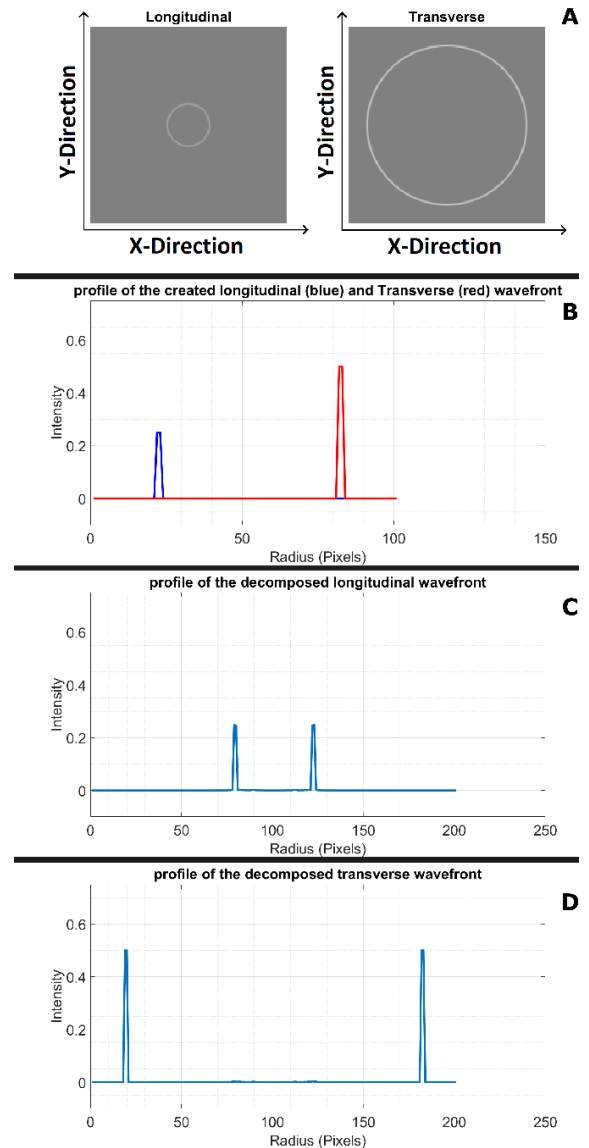
Figure 13. The code output for increased thickness of the longitudinal and transverse waves. A) The image of the completely separated transverse and longitudinal waves. B) Profile of the created transverse and longitudinal waves. C) Profile of the decomposed longitudinal wavefront. D) Profile of the decomposed transverse wavefront

Figure 16 shows that there is a clear pressure wavefront that matches the total displacement map and there is no shear wave, which is also physically accurate. The algorithm really shines in Figure 17, where there is a clear shear wave, which is expected and extracted from the nearly homogenous background. At the same time, the echoed pressure waves create an undetectable overall displacement.

Figure 14. The code output for thinner longitudinal and transverse waves. A) The image of the completely separated transverse and longitudinal waves. B) Profile of the created transverse and longitudinal waves. C) Profile of the decomposed longitudinal wavefront. D) Profile of the decomposed transverse wavefrontz

4. Discussion and Conclusion

We set out to investigate the implementation of Helmholtz decomposition in Fourier space to decompose shear and pressure wavefronts from a displacement vector field. This research is part of a more extensive study evaluating the feasibility of laser-induced shear wave elastography. Several approaches were previously made to separate a mixed elastic wave's transverse and
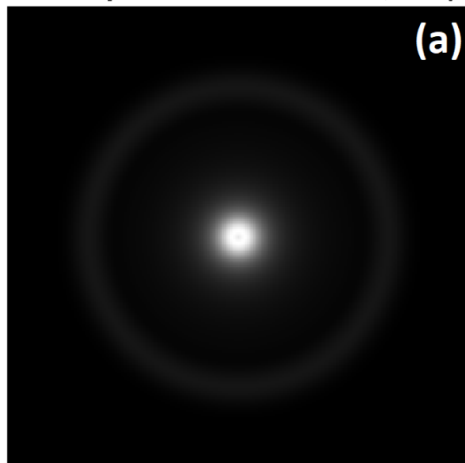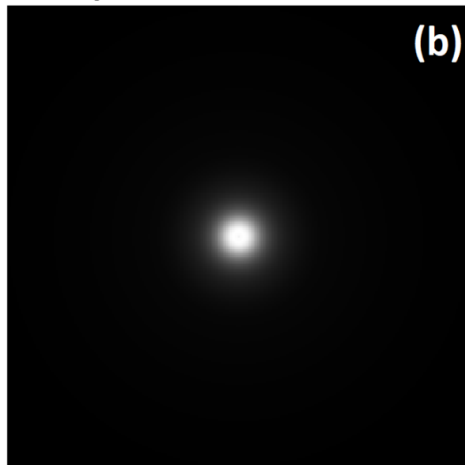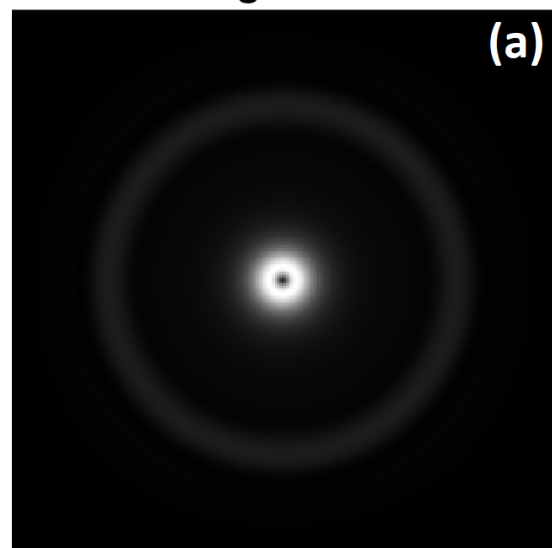
Total displacement Frame 70, 3.1 µs

Total displacement Frame 910, 40.4 µs

Figure 15. Total displacement map of the simulated wave induction, exported from COMSOL. a) Total displacement at 3.1 µs after the induction. The fast pressure wave can be seen in the picture. b) 40.4 µs after the induction, the shear wave should be present but can't be observed due to the background displacement containing echoes and residual waves

Longitudinal

Transverse

Figure 16. Decomposition of the wavefield at 3.1 µs after the wave induction

longitudinal modes. These approaches are mainly rooted in geophysical research, and a lack of data in biomedical research is apparent. Our findings show that the developed algorithm can isolate the shear and pressure components in a vector field.

The final results show that the Code does not interfere with the pure data, and the accuracy of our model is 100% for the shear wave displacements and above 99% for pressure waves. The best and worst results for pressure waves come from tampering with the thickness of the wavefront. It demonstrates the algorithm's dependency on the amount of data it works with; the thicker the wavefront, the more accurately it will be decomposed. However, its ability to isolate shear waves

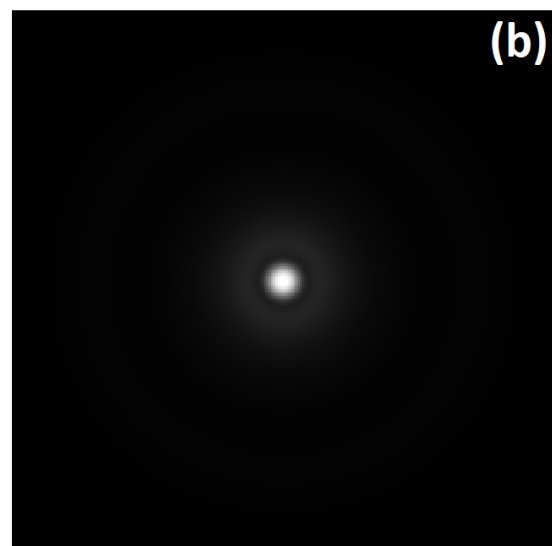is entirely impervious to the thickness of the waves. Moreover, the background noises were kept under 0.03% in every situation, which is astonishing.

Changing the contrast between shear and pressure waves did not alter the accuracy of the algorithm, and the intensity and noise in the final products remained almost the same as the isolated shear wave kept 100% of its amplitude and the amplitude of the pressure wave hovered around 99.6% of its original value. In each step, the Code's performance exceeded 99% accuracy, and the complications such as altered intensity and phase change reported in previous studies were eliminated.
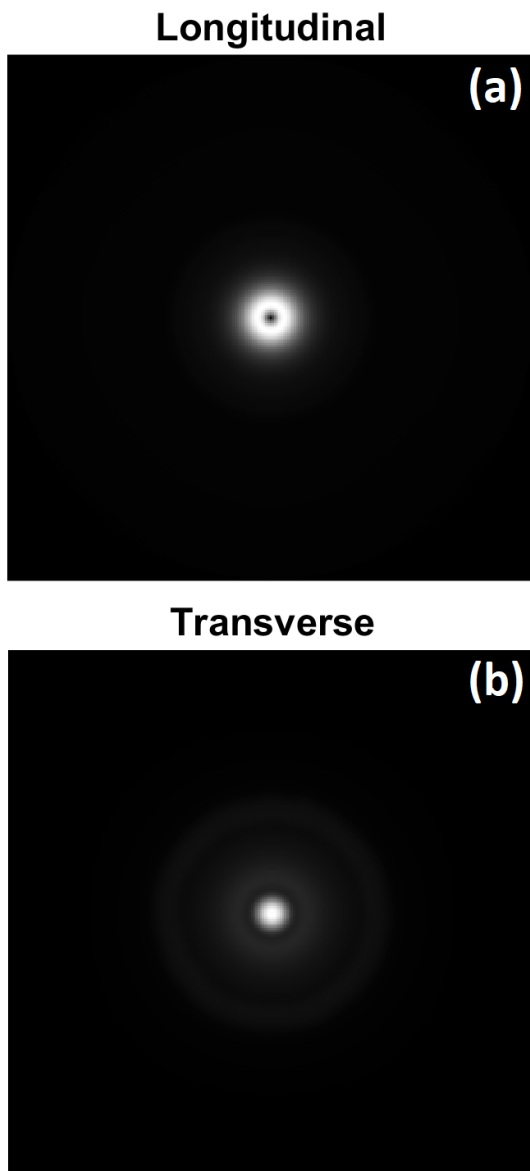
Longitudinal

(a)

Transverse

(b)

Figure 17. a) There are no observable pressure wavefront long after the wave induction Decomposition of the wavefield at 40.4 µs after the wave induction. b) The shear wave can be detected in the picture, which was mixed in the total displacement map in Figure 15

Considering the data has gone through the Fourier transform, mixed with complex values, and underwent a complete decomposition computation, the amount of noise produced in the process seems acceptable.

By feeding the exported data from simulations in COMSOL, the algorithm decomposed the wavefield and demonstrated its value regarding realistic simulations in this field.

In addition, the decomposition process took no more than a few seconds (maximum of 4 seconds) on a typical PC with four processing cores and 16

gigabytes of RAM, with MATLAB 2016b running. It shows that the algorithm has the computational efficiency and speed that was lacking in the previous research mentioned in the introduction.

This research aimed to create a platform to decompose a dataset containing longitudinal and transverse waves. It was a part of a more extensive study to generate a shear wave suitable for shear wave dynamic elastography using COMSOL Multiphysics.

The final product was short, simple, easy to use, and accurate, and has a solid mathematical and physical basis. It can be used to purify the data to its longitudinal or transverse components or can be further developed to perform other tasks.

The most apparent limitation to the team was the absence of external datasets to evaluate the algorithm's validity further.

Moreover, here the longitudinal component is used to calculate the transverse part of the wave. Based on Equations 18 and 19, the number of functions doubles if the transverse wave is decomposed first, which will add to the computation time of the algorithm. However, for further development, it can be restructured to compute the transverse data first.

The Code is available for interested researchers upon request; contact authors for more information.

Acknowledgments

References

1- Wolfgang Sprössig, "On Helmholtz decompositions and their generalizations—an overview." *Mathematical Methods in the Applied Sciences,* Vol. 33 (No. 4), pp. 374-83, (2010).

2- Jia Yan and Paul Sava, "Isotropic angle-domain elastic reverse-time migration." *Geophysics,* Vol. 73 (No. 6), pp. S229-S39, (2008).

3- ROBERT Sun, "Separating P-and S-waves in a prestack 2-dimensional elastic seismogram." in *61st EAGE Conference and Exhibition*, (1999): *European Association of Geoscientists & Engineers*, pp. cp-132-00147.

4- Robert Sun, Jinder Chow, and Kuang-Jung Chen, "Phase correction in separating P-and S-waves in elastic data." *Geophysics,* Vol. 66 (No. 5), pp. 1515-18, (2001).

5- Robert Sun, George A McMechan, Hsu-Hong Hsiao, and Jinder Chow, "Separating P-and S-waves in prestack 3D elastic seismograms using divergence and curl." *Geophysics,* Vol. 69 (No. 1), pp. 286-97, (2004).

6- Robert Sun, George A McMechan, Chen-Shao Lee, Jinder Chow, and Chen-Hong Chen, "Prestack scalar reverse-time depth migration of 3D elastic seismic data." *Geophysics,* Vol. 71 (No. 5), pp. S199-S207, (2006).

7- Xiang Xiao and W Scott Leaney, "Local vertical seismic profiling (VSP) elastic reverse-time migration and migration resolution: Salt-flank imaging with transmitted P-to-S waves." *Geophysics,* Vol. 75 (No. 2), pp. S35-S49, (2010).

8- Qunshan Zhang and George A McMechan, "2D and 3D elastic wavefield vector decomposition in the wavenumber domain for VTI media." *Geophysics,* Vol. 75 (No. 3), pp. D13-D26, (2010).

9- Jiubing Cheng and Sergey Fomel, "Fast algorithms for elastic-wave-mode separation and vector decomposition using low-rank approximation for anisotropic media." *Geophysics,* Vol. 79 (No. 4), pp. C97-C110, (2014).

10- Hejun Zhu, "Elastic wavefield separation based on the Helmholtz decompositionElastic wavefield separation." *Geophysics,* Vol. 82 (No. 2), pp. S173-S83, (2017).

11- Jidong Yang, Hejun Zhu, Wenlong Wang, Yang Zhao, and Houzhu Zhang, "Isotropic elastic reverse time migration using the phase-and amplitude-corrected vector P-and S-wavefields." *Geophysics,* Vol. 83 (No. 6), pp. S489-S503, (2018).

12- Yang Zhao, Houzhu Zhang, Jidong Yang, and Tong Fei, "Reducing artifacts of elastic reverse time migration by the deprimary technique." *Geophysics,* Vol. 83 (No. 6), pp. S569-S77, (2018).

13- Bingluo Gu, Zhiming Ren, Qingqing Li, Jianguang Han, and Zhenchun Li, "An application of vector wavefield decomposition to 3D elastic reverse time migration and field data test." *Computers & Geosciences,* Vol. 131pp. 112-31, (2019).

14- Harsh Bhatia, Gregory Norgard, Valerio Pascucci, and Peer-Timo Bremer, "The Helmholtz-Hodge decomposition—a survey." *IEEE Transactions on visualization and computer graphics,* Vol. 19 (No. 8), pp. 1386-404, (2012).

15- Cherif Amrouche, Christine Bernardi, Monique Dauge, and Vivette Girault, "Vector potentials in three-dimensional non-smooth domains." *Mathematical Methods in the Applied Sciences,* Vol. 21 (No. 9), pp. 823-64, (1998).